# Numerical Model to Predict Hemolysis and Transport in a Membrane-Based Microfluidic Device


## Abstract

Microfluidic devices may overcome the limitations of conventional hemodialysis and oxygenation technology to improve patient outcomes. Namely, the small form of this technology and parallel development of highly permeable membranes may facilitate the development of portable, low-volume, and efficient alternatives to conventional membrane-based equipment. However, the characteristically small dimensions of these devices may also inhibit transport and may also induce flow-mediated nonphysiologic shear stresses that may damage red blood cells (RBCs). *In vitro* testing is commonly used to quantify these phenomenon, but is costly and only characterizes bulk device performance. Here we developed a computational model that predicts the blood damage and solute transport for an abitrary microfluidic geometry. We challenged the predictiveness of the model with three geometric variants of a prototype design and validated hemolysis predictions with *in vitro* blood damge of prototype devices in a recirculating loop. We found that six of the nine tested damage models statistically agree with the experimental data for at least one geometric variant. Additionally, we found that one geometrical variant, the herringbone design, improved toxin (urea) transport to the dialysate by 38% *in silico* at the expense of a 50% increase in hemolysis. Our work demonstrates that computational modeling may supplement *in vitro* testing of prototype microdialyzer/micro-oxygenators to expedite the design optimization of these devices. Furthermore, the low device-induced blood damage measured in our study at physiologically relevant flow rates is promising for the future development of microfluidic dialyzers and oxygenators.


## Introduction

The use of microfluidics in medical devices and artificial organs is increasingly popular and may overcome key limitations in the field of oxygenators and dialyzers. Whereas conventional dialyzers are arranged in a tube-in-tube arrangement, microfluidic devices are commonly arranged in stacked planar plates. This serves as an ideal platform for an emerging class of ultra-high permeability membranes that may dramatically improve the efficacy of these devices, as they yield greater selectivity and permeability than conventional membranes[1]–[4]. A microdevice with an ultra-high permeability membrane for either dialysis or oxygenation may

reduce the required device size and thus blood volume, a critical parameter for smaller patients. Small volume oxygenation of blood for neonatal application can be addressed by microfluidic oxygenators, where it is vital to keep the oxygenator volume appropriately small due to the low blood volume of the neonatal patient. Furthermore, the associated decrease in membrane surface area and blood-contacting artificial materials reduces complications and blood damage[5], [6]. Lastly, miniaturized microfluidic devices are also an important step toward portable dialyzers, which may reduce toxin accumulation in patients, which is associated with patient mortality[1]–[3], [7].

The flow through these oxygenators and dialyzers drives transport of oxygen or toxins, respectively, but may also induce hemolysis, or the rupture of red blood cells (RBCs). At physiologic flow rates, the small dimensions and sharp edges of microdevices may induce shear stresses sufficient to induce hemolysis, leading to anemia, pain, headaches, tachycardia, and changes in blood pressure[8], [9]. Clinically, acute hemolysis is rare in current dialysis treatments, but damage is prevalent in other medical devices that generate supraphysiologic shear. While a clinical target for dialysis-induced hemolysis has not been set, it is important to minimize hemolysis, as the effects can aggregate with frequent treatment and is exacerbated by reduced erythropoietin production commonly found in dialysis patients [8], [10], [11].

Mixing elements incorporated into microfluidic devices have been shown to improve mixing and transport within the fluid by folding streamlines and inducing vortices diffusion, which may improve the efficacy of microdialyzers and micro-oxygenators. The rate of transport of solute in microdevices with ultra-high permeability membranes may be limited by the transfer within the fluid rather than the membrane permeability itself. This manifests as the development of a solute depleted boundary layer within the fluid adjacent to the membrane[3], [4]. This in turn results in a poor diffusion gradient across the membrane, limiting membrane flux and resulting in an overall poor filtration or oxygenation efficiency. Any component of velocity that is perpendicular to the surface acts to move high concentration fluid into the boundary layer, thus replenishing the depleted boundary layer through advection. Herringbone mixers are chevron-shaped steps in the device that induce countercurrent vortices in the flow[12]–[16]. The staggered herringbone mixer is a well-characterized mixing element that has been demonstrated to improve mixing for a wide range of flow regimes ($1 < Re < 100$)[13], [15]. However, it is

unclear whether these flow disturbances caused by mixing elements contribute to flow-induced hemolysis.

Computational modeling is commonly employed to optimize device geometry in parallel with experimental testing and is frequently used in the development of ventricular assist devices[17]–[26] to compare the incremental damage induced by a design variation. Additionally, whereas empirical hemolysis testing results only in overall bulk effects of the device, a spatiotemporal model can determine areas of the device which induce the greatest amount of hemolysis, effectively allowing the designer to "see into" the device. A wide range of blood damage models exist that vary in complexity, but damage is commonly modeled as a function of shear stress $\tau_s$ and exposure time $t$ with parameters fitted to experimental data[17], [19], [23]. Blood damage models of this form have frequently been integrated directly into the framework of a computational fluid dynamics solver, and these methods regularly guide macrofluidic device design, such as pumps, valves, and catheters and may be suitable for the development of micro-oxygenators and micro-dialyzers[18], [22], [25], [26]. To the authors' knowledge, there is no integrated computational framework to predict hemolysis and transport for an arbitrary membrane-based microdevice.

Here we developed an integrated computational model to predict hemolysis and urea transport in a microfluidic hemodialyzer using the ANSYS Fluent computational fluid dynamics package. We challenged the model with three geometric variations (herringbone, reduced gap, and reduced port) of a prototype microdialyzer. We validated the hemolysis model *in vitro* by fabricating prototype devices and measured the hemolysis of the devices in a recirculating blood flow loop. We found that both simulation and experimental results agree that the geometric variations increase the amount of flow-induced hemolysis in the devices and a subset of model predictions statistically agree with experimental data. Furthermore, the herringbone features improved membrane flux by inducing advection near the membrane interface and improved the concentration difference from the inlet to the outlet from 38%.

## Methods/Materials

The computational model of hemolysis and urea transport, including convection through the device and membrane flux, within a microfluidic dialyzer/oxygenator using the native fluid flow solver of ANSYS Fluent. The simulation workflow and communication between the

hemolysis and transport models are shown in Fig. 1. The hemolysis and urea transport terms were defined as species and their transport was governed by the blood or dialysate flow fields. The dialysate computational domain was mathematically coupled to the blood domain through the User Defined Function (UDF) architecture to implement source/sink and convective terms across the membrane, thus allowing species to move across the membrane (Fig. 1). The UDF architecture is additionally used to model hemolysis by treating free hemoglobin (fHb) as a species that is generated as a function of shear stress and is subsequently transported through the computational domain.

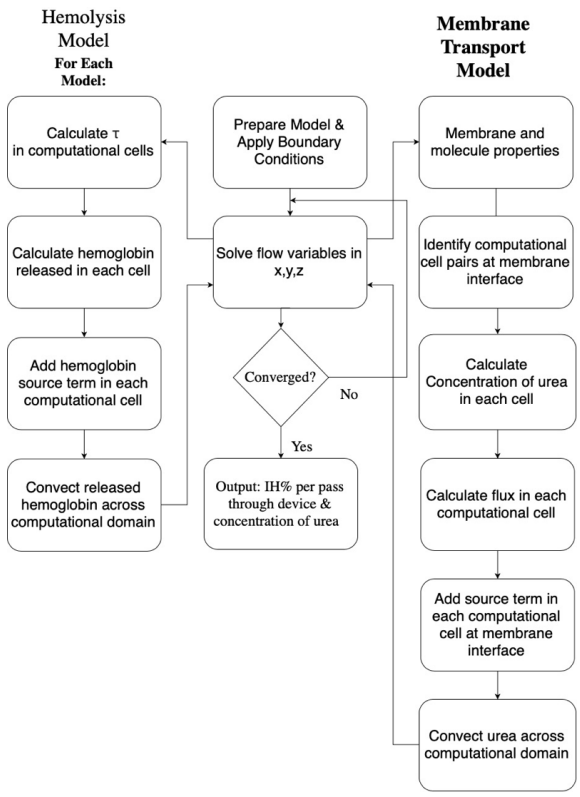


Figure 1: Flow chart of the hemolysis and membrane transport models incorporated via UDFs. Fluent solves for fluid flow using the core algorithms and this illustrated in the center column. Species are advected. Hemoglobin is treated as a species with a source term that allows for the generation of hemolysis from shear stresses.

The simulation boundary conditions are described in Fig. 2A. For these particular experiments, flow rates were set at 100 ml/min for both blood and dialysate. The blood side inlet was set to an arbitrary concentration of urea and zero free hemoglobin. A fully-developed parabolic velocity

profile is specified at both inlets to avoid non-physical wall shear stress and associated hemolysis. The hemolysis accumulated in a single pass through the device is quantified by the free hemoglobin at the outlet. Transport is quantified as the relative urea concentration at the outlet of the dialysate side.

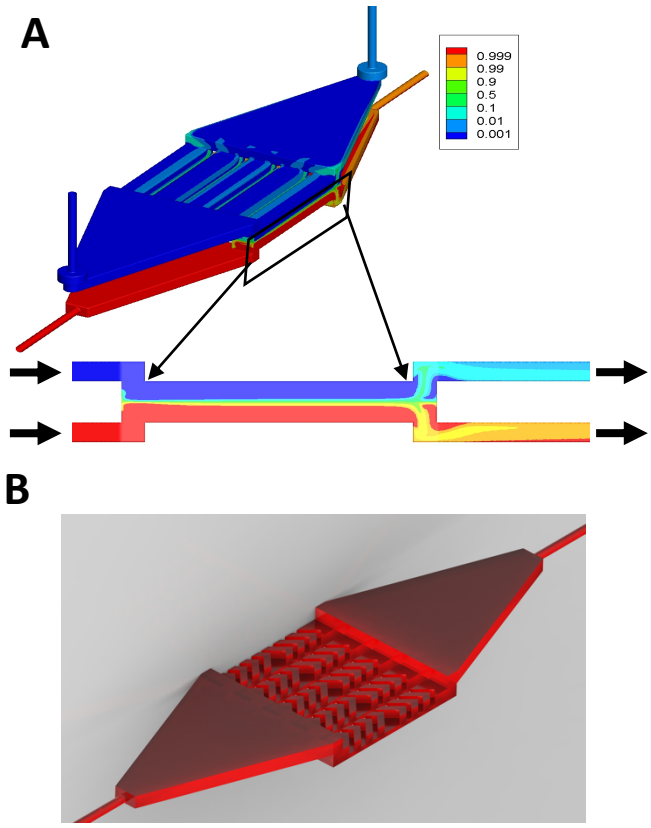


Figure 2: A) Geometry showing blood side (red) and dialysate side (blue) of a prototype microdialyzer. Contours are the concentration of urea. The flow rate was set to 100 mL/min B) Herringbone mixers in a prototype microdevice.

Three geometrical variants of prototype microdevices are simulated (Fig. 2A) and validated *in vitro* to explore the model's predictive power of both absolute magnitude and sensitivity to geometry variations (Table 1). All of the devices have an inlet and outlet manifold that transitions from the circular port to the channels at the membrane interface. Information about the properties of each device can be found in Table S1. The computational and experimental results were compared. Furthermore, one device was equipped with herringbone mixers to explore their impact on hemolysis and membrane flux (Fig. 2B).

For each simulation case, a mesh convergence study was performed using Richardson Extrapolation to assess mesh discretization error[27], [28]. For each simulation condition, the solution was resolved for three mesh sizes: 80, 113, and 160 $\mu$m CutCell (hexahedral) elements (fine, medium, and coarse mesh size respectively). Mesh refinement regions proportional to the base mesh size were specified for areas with high-velocity gradients to improve solution accuracy and convergence. Grid order suggests that grid-induced error is sufficiently low (<5% average for all models). For these cases, the 80 micron mesh was used. The shallow channel of the reduced gap device (250 $\mu$m) required an element size that is even more refined (57 $\mu$m) to reach a converged solution. Each mesh contained approximately 24M hexahedral computational cells the finest resolution.

| | Baseline | Herringbone | Reduced Port | Reduced Gap |
|---|---|---|---|---|
| **Herringbone Mixers** | No | Yes | No | No |
| **# of Channels** | 5 | 5 | 5 | 2 |
| **Channel Width (mm)** | 1.66 | 1.66 | 1.66 | 1.66 |
| **Channel Height (mm)** | 2.8 | 2.8 | 2.8 | 0.25 |
| **Port Size** | 1.6 | 1 | 1.6 | 1.6 |

Table 1: Properties of the devices tested *in silico* and *in vitro*.

**Hemolysis Model**

Scalar shear stress is calculated in each computational element. The hemolysis ratio is subsequently calculated as a proxy for free hemoglobin in each computational cell as a function of the prescribed hemolysis model. The blood damage per pass through the device is calculated as the average hemolysis ratio at the device outlet. Consistent with prior methods[23], the hemolysis ratio is treated as a species of solute within the model, which then allows the continuity equation to be solved at each computational cell in the domain.

$$\frac{\partial}{\partial x_i}\left(\rho u_i \phi_k - \Gamma \frac{\partial \phi_k}{\partial x_i}\right) = S_{\phi_k}$$

The two terms on the left side of the equation represent the advective and diffusive terms. The source term $S_{\phi_k}$, defined by the UDF, describes the generation of hemolysis due to shear stresses. The time history model differs from the power law model in that it considers an RBC's

"history" of hemolysis; RBCs that have previously experienced shear stress will release less hemoglobin upon subsequent exposure to the same shear, which better mimics physiologic observations. Within each class of hemolysis models, the three calibrated parameter sets, the Giersiepen (Models 1-3), Heuser/Optiz (Models 4-6), and Zhang (Models 7-9) were considered in our study[29]–[31]. For each of these parameter sets, hemolysis was calculated using one of three methods of computing the scalar shear stress based on the viscous stress tensor reported by Fluent for each computational cell. For each of these parameter sets, hemolysis was calculated using one of three methods of computing the scalar shear stress based on either the second stress invariant ($\tau_{vm}$ and $\tau_p$) or the viscous stress tensor ($\tau_b$) for a total of eighteen damage models. $\tau_p$ is the square root of the absolute value of the second stress invariant of the deviatoric stress tensor[32], [33]. $\tau_{vm}$ is the von mises stress of this stress tensor, or simply $\tau_p$ multiplied by the square root of 3[20], [34]. $\tau_b$ is computed from the off-diagonal components of this stress tensor as shown in Bludszuweit et al. [34]. The equations and parameters for each model are summarized in Table S2.

**Membrane Transport Model**

The diffusion of a molecule through a porous medium was modeled based on the molecule-specific permeability through the membrane according to Eq 8. The properties of urea and the membrane used in this work are listed in Table S3. The flux $J_i$ through an adjacent cell pair $i$ at the membrane is described by Fick's First Law for each timestep, where $D_m$ represents the calculated membrane diffusivity and $\Delta C$ is the concentration gradient across the paired cells.

$$J_i = D_m \Delta C$$

The membrane transport model computes the flux between computational cell pairs on opposing sides of the membrane. The concentration of urea is normalized to a value of 0 to 1, where 1 corresponds to the concentration at the inlet of the blood-side. The mass-weighted concentration is computed at the outlet concentration and the concentration from the inlet to outlet is then calculated and used as the scalar metric of overall transport. Membrane flux was quantified by comparing the change in concentration of urea from the inlet to the outlet of the blood-side of the device. A higher change in concentration indicates that diffusion across the membrane is greater.

**Hemolysis Experimentation**

We fabricated prototype microfluidic and developed a recirculating loop to measure hemolysis induced by the devices. Blood circulated through these circuits at 100 mL/min to match our simulations and hemolysis was measured every 30 minutes. Linear regression was used to calculate the IH% per pass through the device.Whole bovine calf blood with Anticoagulant Citrate Dextrose (ACD) was acquired through venipuncture (Lampire Biological Laboratories, PA) from four or five distinct animals, each considered separate biological replicates.

Blood was shipped in a refrigerated container and used within 12 hours of receipt. Blood was filtered through a 250 micron pore mesh (McMaster Carr) to remove any thrombus formation. The circuits were constructed of polycarbonate fittings (VWR) and silicone tubing (MasterFlex), Figure 3. Flow through the circuit was driven by a peristaltic pump (MasterFlex) with multiple drive heads attached to permit parallel testing of devices with the same blood donor (3A-B). The pump speed is calibrated to 100 mL/min to match simulations. The circuits are filled with 1X Phosphate Buffered Saline (PBS) and circulated for 20 minutes according to standardized hemolysis testing protocols[35]. The PBS was subsequently removed and 75 mL blood was immediately infused into the circuits via a syringe pump.

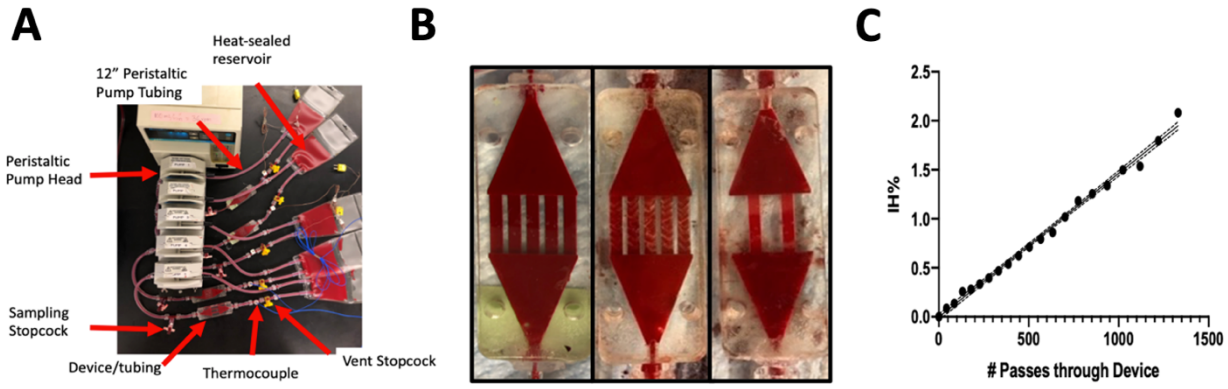


Figure 3: A) Photograph of the five parallel blood circuits connected in parallel with multiple peristaltic pump heads and is used in experimentation. B) Examples of physical devices used in experimentation: reduced port, herringbone, and reduced gap microdevices from left to right. C) Example data set showing measured IH at each time point, corresponding to # of passes through the device, and regressed line to determine damage per pass.

196 Two replicate samples were aspirated from the circuit every 30 minutes for 10-12 hours.
197 These samples were centrifuged at 3,000g for 10 minutes to separate plasma from RBCs. The
198 plasma was separated and centrifuged at 13,000g for 10 minutes to remove any remaining cells.
199 200 uL of resulting plasma was plated into a 96-well plate and the absorbance is measured at
200 560, 576, and 593 nm wavelengths. Hemolysis was determined from the absorbance
201 measurements according to the Cripps method. The index of hemolysis was computed by
202 accounting for the hematocrit[26]. The number of passes was calculated with consideration of
203 circuit volume and flow rate.

204 **Comparison of Experiment to Computation**

205 IH% per pass from each of the eighteen variations of the hemolysis model were compared to
206 experimental data. Regression analysis is performed on the curve of IH% vs. the number of
207 cumulative passes (flow rate divided by system volume) to determine the IH% per pass (Fig 3C).
208 Damage induced by a feature (herringbone, reduced port, or reduced gap) was calculated as the
209 difference between that device loop hemolysis per pass and the baseline featureless device
210 (referred to as incremental damage). The device IH% per pass was calculated by subtracting the
211 baseline damage per pass from the device circuit damage per pass. The model agreement was
212 assessed using Student's one-sample t-test ($p<0.05$) was used to identify any cases in which the
213 experimental and simulation results were not statistically different.

214 **RESULTS**

215 **Implementation and validation of Computational Model**

216 The implementation of the membrane transport model as a UDF was validated against a
217 known analytical solution in a representative geometry (Fig. S1). Similarly, the results of shear-
218 induced damage for a simplified flow with known and constant shear agreed with an analytical
219 solution, indicating correct implementation of the hemolysis models. While the magnitude of
220 hemolysis is different for each model and device, there is little difference between power law and
221 time-history models (Fig. 4A), so only power law model data is referred to from here forward.

222 We fabricated and tested four prototype microdialyzers: a baseline device and three
223 geometrical variants with either reduced ports, herringbone features, or a reduced gap at the

membrane. The *in vitro* hemolysis (IH%) per pass damage was determined from linear regression of hemolysis from blood circulating over 1400 times through the microdevices. Interestingly, all three device modifications yielded similar increases in hemolysis over the baseline device a statistically significant difference between the baseline/herringbone devices (p=0.043) and baseline/reduced port devices (p=0.029) but not the baseline/reduced gap devices (p=0.075), as shown in Fig. 4B.

The magnitude of damage predicted by the various numerical models for a single geometry varies drastically (Fig. 4C), with an overall range of two orders of magnitude difference (Model 3 vs. 5 in 4C). The strongest effect is a result of the $C, \alpha, and\ \beta$ parameters derived from the literature, with Giersiepen (Models 1-3) predicting the highest damage and Heuser-Opitz (Models 4-6) the lowest. The means of calculating shear has a weaker, but still significant, effect on the prediction with $\tau_p$ shear model consistently predicting 4 times greater hemolysis per pass than the $\tau_b$ shear model. All models are consistent in predicting the relative changes between devices (Fig. 4C), namely the herringbones increase hemolysis per pass through the device ~10% and all models predict the smaller ports and high shear devices are predicted to induce a 10 to 20-fold increase in hemolysis compared to the featureless device (not shown).

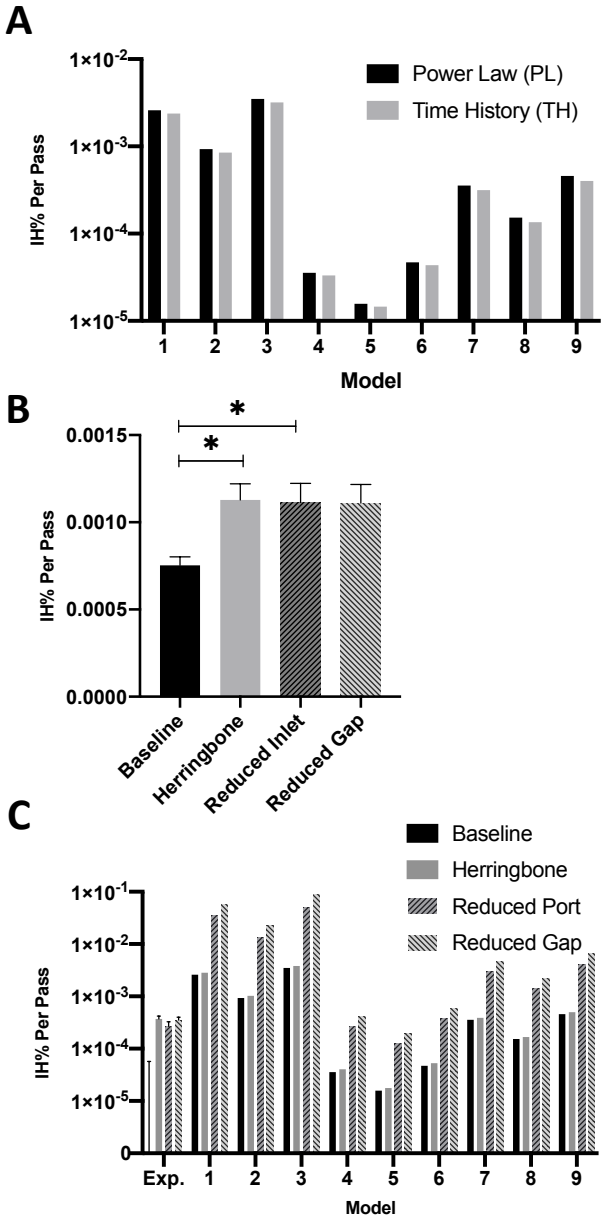


Figure 4: A) Comparison of simulation data for the featureless (baseline) device for all 18 numerical models with Giersiepen parameters (Models 1-3), Heuser/Optiz parameters (Models 4-6), and the Zhang parameters (Models 7-9). B) Raw experimental data comparing IH% per pass for each device. C) Experimental and simulation data for the 9 power law numerical models for all four devices. * indicates statistical significance of $p<0.05$ (Kruskal-Wallis).

**Computational models consistently predict relative, but not absolute, hemolysis.**

We next examined whether the hemolysis models could predict the difference in hemolysis between the baseline device and modified microfluidic devices. We compared the differences between the simulation and experimental data by calculating the $log_{10}$ fold change between the simulation and experimental data for the absolute difference between the modified and baseline hemolysis (incremental damage) in which model overpredictions are indicated in red and model underpredictions are indicated as blue (Fig. 5A). The absolute incremental damage is the difference in hemolysis per pass of the baseline devices subtracted from the modified devices, whereas the relative incremental damage is the ratio of the modified device hemolysis per pass to the baseline device hemolysis per pass.

**A**

| | Hemolysis Model | | | | | | | | |
|---|---|---|---|---|---|---|---|---|---|
| | 1 | 2 | 3 | 4 | 5 | 6 | 7 | 8 | 9 |
| **Reduced Ports** | 2.0 | 1.5 | 2.1 | -0.2 | -0.5 | 0.0 | 0.9 | 0.5 | 1.0 |
| **Herringbone** | -0.2 | -0.6 | -0.1 | -1.9 | -2.3 | -1.8 | -1.1 | -1.4 | -1.0 |
| **Reduced Gap** | 2.2 | 1.8 | 2.4 | 0.0 | -0.3 | 0.2 | 1.1 | 0.8 | 1.2 |

Overprediction
2
0
-2
Underprediction

**B**

| | Hemolysis Model | | | | | | | | |
|---|---|---|---|---|---|---|---|---|---|
| | 1 | 2 | 3 | 4 | 5 | 6 | 7 | 8 | 9 |
| **Reduced Ports** | | | | 0.35 | 0.11 | 0.78 | | | |
| **Herringbone** | 0.28 | 0.05 | 0.69 | | | | | | |
| **Reduced Gap** | | | | 0.88 | 0.21 | 0.18 | | | |

Figure 5: A) $log_{10}$ transformed fold change between the simulation and experimental results for the incremental damage. B) Agreement between the simulation and model. Statistical agreement ($p<0.05$) is indicated in green with the corresponding p-value for each model and device (one-sample t test).

Comparison of the fold change in incremental damage reveals that the models consistently underpredict the difference in hemolysis between the herringbone incremental damage for all blood damage models (Fig. 5A). For both the reduced port and reduced gap devices, some blood damage models overpredicted (PL-1, -2, -3, -7, -8, and -9), while other damage models underpredicted the hemolysis (PL-4, and -5). We next asked whether any model predictions statistically agreed with the experimental data. To this end, we performed one-sample t-tests to compare the simulation and experimental incremental damage. The PL-4, -5, and -6

models were statistically similar ($p>0.05$) for the reduced port and reduced gap devices and the PL-1, -2, and -3 models were statistically similar to the herringbone incremental damage (Fig. 5B).

**Herringbones improve membrane flux by disturbing flow near the membrane**

Streamlines in the smooth, reduced port, and reduced gap devices are all nearly straight and parallel to the membrane channel, whereas the streamlines in the herringbone device have more swirling motion characterized by motion perpendicular to the membrane (Fig. 6). The herringbone devices achieved a greater change in urea concentration as a result of greater membrane flux at the membrane interface (18% to 25%). These data suggest that the herringbones disturb flow near the membrane interface to induce advection-mediated replenishment of the urea boundary layer at the membrane. This results in greater transport than diffusion-mediated transport in the baseline device.

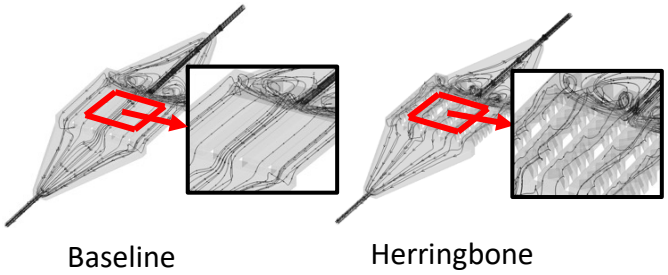


Figure 6: Comparison of the streamlines in the baseline and herringbone device. Chaotic streamlines proximal to the membrane are present in the herringbone device but not the baseline device.

**Discussion**

Models of membrane transport and hemolysis, both of which are critical to dialysis and oxygenation devices, can be simultaneously implemented into a single computational model to supplement *in vitro* experimental testing to accelerate design development and optimization. This work suggests that computational modeling can predict blood damage in these devices, which may be paramount in device design; however, additional experimentation is necessary to determine the parameter space in which the model may predict accurately. To this end, multiple flow rates and a range of device geometries may be tested to further examine this predictive

range. The benefits of modeling have been observed in VAD design, in which computational modeling plays a significant role in the iterative development of blood pumps. While the optimization of these devices is not explored in this work, it is a powerful tool that may drive the performance improvement and clinical adoption of microfluidic dialyzers and oxygenators.

The models predicted hemolysis values across several orders of magnitude, which is consistent with the literature[23]. Furthermore, models that differ only by the scalar shear stress calculation (Models 1-3, 4-6, and 7-9) predict similar levels of hemolysis, suggesting that the prediction is less sensitive to the scalar shear stress model compared to the other model parameters ($C, \alpha, \beta$). Specifically, the Giersiepen parameters have been cited as significantly overpredicting hemolysis[23]. We also compared the incremental damage, or the difference in IH% per pass of the modified devices minus the baseline device. Interestingly, the Giersiepen models best predicted the difference between the baseline and herringbone devices and the Heuser/Optiz parameters best predicted the difference between the other two modified devices compared to the baseline device. These findings support observations in the literature that the Heuser/Optiz parameters best agree with experimental measurements of hemolysis[23]. The use of the time-history model may not be warranted for this and similar geometries. It is substantially more difficult to implement, somewhat more computationally expensive, and results in no significant improvement in accuracy of prediction. This is expected because the time-history effect should be small since the magnitude of hemolysis predicted is also low.

The model was sensitive to each of the three design changes introduced and predicted an increase in hemolysis for all three, with the largest incremental increase resulting from the two designs intended to increase shear (reduced port and reduced gap). Hemolysis increased modestly as a result of the introduction of herringbones, but it also increased transport, as measured by the change in concentration from the inlet of the device to the outlet (18% to 25%). Improved transport may also allow the device to operate at decreased flow rate, subsequently decreasing shear stresses and therefore hemolysis in the microdevice. These parameters could be optimized *in silico* in future studies. The proposed herringbone geometry in this work was adapted from the literature, so optimization of the herringbone features and channel geometry for this application may further improve the benefit of the herringbone mixers.

The minimal device induced damage within all devices indicates promise for clinical use. The baseline device damage was very small (<0.0001% per pass) and not statistically different from a device-free control loop (N=4). The damage from the pump and associated tubing (~0.003%/pass) was at about one order of magnitude larger than the damage from all devices (~0.0003%). This results in a low signal-to-noise ratio in experimentation, but the low device induced hemolysis is promising for the future clinical use of microfluidic blood-contacting devices. Although these devices contain sharp edges and small features that induce non-physiological shear stresses at the tested flow rates, these stresses appear insufficient to induce significant hemolysis in the devices. The experimental conditions (flow rate: 100 mL/min, reservoir volume: 75 mL, experiment length: 10-12 hours) were specified to maximize the hemolysis signal from the devices to make it measurable. These conditions generate over 1400 passes through the devices, over one order of magnitude greater than those of current intermittent dialysis[9]. The number of passes through the device in these experiments may greatly exceed what would normally be experienced if used clinically as a wearable continuous flow device. For example, cells from a person with 6L total blood volume would pass through the device about 24 times per day, resulting in total daily damage of <0.01%. This is orders of magnitude below the 2-5% at which symptoms of toxicity occur [9], and does not account for filtration of free hemoglobin by the body.

These data also call into question the hemolysis induced by pumps and tubing typical of these devices and experimental protocols. Sakota et al. studied hemodialysis-induced hemolysis by measuring hemolysis in a blood circuit at clinically-relevant flow rates and volumes [9]. Their experimental setup also included cannulas that connect the patient's blood vessels. These cannulas have been studied experimentally and computationally as another source of hemolysis in hemodialysis[8], [11], [18], [23], [36]. The diameter and flow rate determine the shear stresses and thus hemolysis induced by the cannula. Multiple cannulas (double cannula hemodialysis) may be used[9] to reduce the flow rate through each cannula to induce less hemolysis overall.

## Conclusion

Fundamentally, hemolysis and other shear-induced blood damage are caused by the high flow rates required to remove toxins from the blood in a relatively short treatment time (4 hours).

Longer treatments at reduced flow rates, afforded by continuously filtering the blood, may dramatically reduce device induced hemolysis. Our study indicates great promise for the use of microfluidic devices with highly permeable membranes for dialysis or oxygenation. Further, the study indicates the promise of an integrated computational model that includes both transport and hemolysis to guide the iterative design process required to develop these devices.

357 References:


358 [1] D. G. Johnson *et al.*, "Ultrathin Silicon Membranes for Wearable Dialysis," *Adv. Chronic*
359 *Kidney Dis.*, vol. 20, no. 6, pp. 508–515, 2013.

360 [2] J. J. Miller *et al.*, "Free Standing, Large-Area Silicon Nitride Membranes for High Toxin
361 Clearance in Blood Surrogate for Small-Format Hemodialysis," *Membranes (Basel).*, vol.
362 10, no. 6, p. 119, Jun. 2020.

363 [3] K. Hill *et al.*, "Second Generation Nanoporous Silicon Nitride Membranes for High Toxin
364 Clearance and Small Format Hemodialysis," *Adv. Healthc. Mater.*, vol. 9, no. 4, Feb.
365 2020.

366 [4] C. C. Striemer, T. R. Gaborski, J. L. McGrath, and P. M. Fauchet, "Charge- and size-
367 based separation of macromolecules using ultrathin silicon membranes," *Nature*, vol. 445,
368 no. 7129, pp. 749–753, Feb. 2007.

369 [5] R. P. Rode, H. H. Chung, H. N. Miller, T. R. Gaborski, and S. Moghaddam, "Bilayer
370 graphene oxide membranes for a wearable hemodialyzer."

371 [6] M. Dabaghi *et al.*, "An artificial placenta type microfluidic blood oxygenator with double-
372 sided gas transfer microchannels and its integration as a neonatal lung assist device,"
373 *Biomicrofluidics*, vol. 12, no. 4, p. 44101, 2018.

374 [7] T. Burgin, D. Johnson, H. Chung, A. Clark, and J. McGrath, "Analytical and finite
375 element modeling of nanomembranes for miniaturized, continuous hemodialysis,"
376 *Membranes (Basel).*, vol. 6, no. 1, pp. 1–14, 2015.

377 [8] H. D. Polaschegg, "Red blood cell damage from extracorporeal circulation in
378 hemodialysis," *Seminars in Dialysis*, vol. 22, no. 5. John Wiley & Sons, Ltd (10.1111),
379 pp. 524–531, 01-Sep-2009.

380 [9] R. Sakota, C. A. Lodi, S. A. Sconziano, W. Beck, and J. P. Bosch, "In Vitro Comparative
381 Assessment of Mechanical Blood Damage Induced by Different Hemodialysis
382 Treatments," *Artif. Organs*, vol. 39, no. 12, pp. 1015–1023, Dec. 2015.

383 [10] B. P. Resource, "Blood Basics," 2012. [Online]. Available:
384 https://www.hematology.org/Patients/Basics/. [Accessed: 01-Jul-2019].

385 [11] D. De Wachter and P. Verdonck, "Numerical calculation of hemolysis levels in peripheral
386 hemodialysis cannulas," *Artif. Organs*, vol. 26, no. 7, pp. 576–582, Jul. 2002.

387 [12] P. J. Shah, M. Dimaki, and W. E. Svendsen, "A novel passive microfluidic device for

preprocessing whole blood for point of care diagnostics," *TRANSDUCERS 2009 - 15th Int. Conf. Solid-State Sensors, Actuators Microsystems*, pp. 417–420, 2009.

[13] A. D. Stroock, S. K. W. Dertinger, A. Ajdari, I. M. Mezic´, H. A. Stone, and G. M. Whitesides, "Chaotic Mixer for Microchannels."

[14] T. Femmer, M. L. Eggersdorfer, A. J. C. Kuehne, and M. Wessling, "Efficient gas-liquid contact using microfluidic membrane devices with staggered herringbone mixers," *Lab Chip*, vol. 15, no. 15, pp. 3132–3137, 2015.

[15] M. S. Williams, K. J. Longmuir, and P. Yager, "A practical guide to the staggered herringbone mixer," *Lab Chip*, vol. 8, no. 7, pp. 1121–1129, 2008.

[16] R. Nasr Isfahani, S. Bigham, M. Mortazavi, X. Wei, and S. Moghaddam, "Impact of micromixing on performance of a membrane-based absorber," *Energy*, vol. 90, pp. 997–1004, 2015.

[17] M. E. Taskin, K. H. Fraser, T. Zhang, C. Wu, B. P. Griffith, and Z. J. Wu, "Evaluation of Eulerian and Lagrangian models for hemolysis estimation," *ASAIO J.*, vol. 58, no. 4, pp. 363–372, 2012.

[18] A. Garon and M. I. Farinas, "Fast three-dimensional numerical hemolysis approximation," *Artif. Organs*, vol. 28, no. 11, pp. 1016–1025, 2004.

[19] L. Goubergrits, U. Kertzscher, and M. Lommel, "Past and future of blood damage modelling in a view of translational research," *International Journal of Artificial Organs*, 2018.

[20] C. Bludszuweit, "Model for a General Mechanical Blood Damage Prediction," *Artif. Organs*, vol. 19, no. 7, pp. 583–589, 1995.

[21] K. K. Yeleswarapu, J. F. Antaki, M. V Kameneva, and K. R. Rajagopal, "A Mathematical Model for Shear-Induced Hemolysis," *Artif. Organs*, vol. 19, no. 7, pp. 576–582, 1995.

[22] U. Morbiducci, G. Di Benedetto, M. Grigioni, C. Del Gaudio, and G. D'Avenio, "A novel formulation for blood trauma prediction by a modified power-law mathematical model," *Biomech. Model. Mechanobiol.*, vol. 4, no. 4, pp. 249–260, 2005.

[23] H. Yu, S. Engel, G. Janiga, and D. Thévenin, "A Review of Hemolysis Prediction Models for Computational Fluid Dynamics," *Artif. Organs*, vol. 41, no. 7, pp. 603–621, Jul. 2017.

[24] R. A. Malinauskas *et al.*, "FDA Benchmark Medical Device Flow Models for CFD Validation," *ASAIO J.*, vol. 63, no. 2, pp. 150–160, 2017.

[25] L. Goubergrits, “Numerical modeling of blood damage: Current status, challenges and future prospects,” *Expert Review of Medical Devices*, vol. 3, no. 5, pp. 527–531, 2006.

[26] T. Zhang *et al.*, “Study of flow-induced hemolysis using novel couette-type blood-shearing devices,” *Artif. Organs*, vol. 35, no. 12, pp. 1180–1186, Dec. 2012.

[27] P. J. Roache, “Perspective: A Method for Uniform Reporting of Grid Refinement Studies,” *J. Fluids Eng.*, vol. 116, no. 3, p. 405, 1994.

[28] P. J. Roache, “Quantification of Uncertainty in Computational Fluid Dynamics,” 2002.

[29] T. Zhang and M. E. Taskin, “Study of flow- induced hemolysis using novel Couette-type blood-shearing devices,” *Artif. Organs*, no. 35, pp. 1180–1186, 2011.

[30] M. Giersiepen, L. Wurzinger, R. Opitz, and H. Reul, “Estimation of shear stress-related blood damage in heart valve prostheses—in vitro comparison of 25 aortic valves,” *Int. J. Artif. Organs*, no. 13, pp. 300–306, 1990.

[31] G. Heuser and R. Opitz, “A Couette viscometer for short time shearing of blood,” *Biorheology*, no. 17, pp. 17–24, 1980.

[32] L. Pauli, J. Nam, M. Pasquali, and M. Behr, “Transient stress-based and strain-based hemolysis estimation in a simplified blood pump,” *Int. j. numer. method. biomed. eng.*, vol. 29, no. 10, pp. 1148–1160, 2013.

[33] M. I. Farinas, A. Garon, D. Lacasse, and D. N’dri, “Asymptotically consistent numerical approximation of hemolysis,” *J. Biomech. Eng.*, vol. 128, no. 5, pp. 688–696, 2006.

[34] C. Bludszuweit, “Three-Dimensional Numerical Prediction of Stress Loading of Blood Particles in a Centrifugal Pump,” *Artif. Organs*, vol. 19, no. 7, pp. 590–596, Jul. 1995.

[35] “ASTM F1841-97.” [Online]. Available: www.astm.org,. [Accessed: 02-Jul-2019].

[36] E. Raymond, D. S. De Wachter’, P. R. Verdonck’, J. Y. De Vos2, and R. O. Hombrouckx, “Blood trauma in plastic haemodialysis cannulae,” 1997.

[37] J. Winkelmann, “Diffusion coefficient of water-t into water and urea solution,” 2017, p. 1617.

[38] L. A. Stevens, C. Huang, and A. S. Levey, “Measurement and Estimation of Kidney Function,” in *Chronic Kidney Disease, Dialysis, and Transplantation*, 2010, pp. 22–38.

**Supplemental Data**

| Model Name | Governing Equation | Shear Stress Model | Parameter Set | C | $\alpha$ | $\beta$ |
|---|---|---|---|---|---|---|
| PL-1 | $D(\tau,t)=\frac{\Delta fHb}{Hb}=C\tau^{\alpha}t^{\beta}$ | $\tau_{vm}$ | Giersiepen | $3.63\times10^{-7}$ | 2.416 | 0.785 |
| PL-2 | $D(\tau,t)=\frac{\Delta fHb}{Hb}=C\tau^{\alpha}t^{\beta}$ | $\tau_{b}$ | Giersiepen | $3.63\times10^{-7}$ | 2.416 | 0.785 |
| PL-3 | $D(\tau,t)=\frac{\Delta fHb}{Hb}=C\tau^{\alpha}t^{\beta}$ | $\tau_{p}$ | Giersiepen | $3.63\times10^{-7}$ | 2.416 | 0.785 |
| PL-4 | $D(\tau,t)=\frac{\Delta fHb}{Hb}=C\tau^{\alpha}t^{\beta}$ | $\tau_{vm}$ | Heuser/Opitz | $1.80\times10^{-8}$ | 1.991 | 0.765 |
| PL-5 | $D(\tau,t)=\frac{\Delta fHb}{Hb}=C\tau^{\alpha}t^{\beta}$ | $\tau_{b}$ | Heuser/Opitz | $1.80\times10^{-8}$ | 1.991 | 0.765 |
| PL-6 | $D(\tau,t)=\frac{\Delta fHb}{Hb}=C\tau^{\alpha}t^{\beta}$ | $\tau_{p}$ | Heuser/Opitz | $1.80\times10^{-8}$ | 1.991 | 0.765 |
| PL-7 | $D(\tau,t)=\frac{\Delta fHb}{Hb}=C\tau^{\alpha}t^{\beta}$ | $\tau_{vm}$ | Zhang | $1.228\times10^{-7}$ | 1.9918 | 0.6606 |
| PL-8 | $D(\tau,t)=\frac{\Delta fHb}{Hb}=C\tau^{\alpha}t^{\beta}$ | $\tau_{b}$ | Zhang | $1.228\times10^{-7}$ | 1.9918 | 0.6606 |
| PL-9 | $D(\tau,t)=\frac{\Delta fHb}{Hb}=C\tau^{\alpha}t^{\beta}$ | $\tau_{p}$ | Zhang | $1.228\times10^{-7}$ | 1.9918 | 0.6606 |
| TH-1 | $D(\tau,t)=\frac{\Delta fHb}{Hb}=\sum_{i=inlet}^{i}C\beta\left[\sum_{j=1}^{j_i}\tau_{i_j}^{\alpha}\Delta t_j\right]^{\beta-1}\times\tau_{i_i}^{\alpha}\Delta t_i$ | $\tau_{vm}$ | Giersiepen | $3.63\times10^{-7}$ | 2.416 | 0.785 |
| TH-2 | $D(\tau,t)=\frac{\Delta fHb}{Hb}=\sum_{i=inlet}^{i}C\beta\left[\sum_{j=1}^{j_i}\tau_{i_j}^{\alpha}\Delta t_j\right]^{\beta-1}\times\tau_{i_i}^{\alpha}\Delta t_i$ | $\tau_{b}$ | Giersiepen | $3.63\times10^{-7}$ | 2.416 | 0.785 |
| TH-3 | $D(\tau,t)=\frac{\Delta fHb}{Hb}=\sum_{i=inlet}^{i}C\beta\left[\sum_{j=1}^{j_i}\tau_{i_j}^{\alpha}\Delta t_j\right]^{\beta-1}\times\tau_{i_i}^{\alpha}\Delta t_i$ | $\tau_{p}$ | Giersiepen | $3.63\times10^{-7}$ | 2.416 | 0.785 |
| TH-4 | $D(\tau,t)=\frac{\Delta fHb}{Hb}=\sum_{i=inlet}^{i}C\beta\left[\sum_{j=1}^{j_i}\tau_{i_j}^{\alpha}\Delta t_j\right]^{\beta-1}\times\tau_{i_i}^{\alpha}\Delta t_i$ | $\tau_{vm}$ | Heuser/Opitz | $1.80\times10^{-8}$ | 1.991 | 0.765 |
| TH-5 | $D(\tau,t)=\frac{\Delta fHb}{Hb}=\sum_{i=inlet}^{i}C\beta\left[\sum_{j=1}^{j_i}\tau_{i_j}^{\alpha}\Delta t_j\right]^{\beta-1}\times\tau_{i_i}^{\alpha}\Delta t_i$ | $\tau_{b}$ | Heuser/Opitz | $1.80\times10^{-8}$ | 1.991 | 0.765 |
| TH-6 | $D(\tau,t)=\frac{\Delta fHb}{Hb}=\sum_{i=inlet}^{i}C\beta\left[\sum_{j=1}^{j_i}\tau_{i_j}^{\alpha}\Delta t_j\right]^{\beta-1}\times\tau_{i_i}^{\alpha}\Delta t_i$ | $\tau_{p}$ | Heuser/Opitz | $1.80\times10^{-8}$ | 1.991 | 0.765 |
| TH-7 | $D(\tau,t)=\frac{\Delta fHb}{Hb}=\sum_{i=inlet}^{i}C\beta\left[\sum_{j=1}^{j_i}\tau_{i_j}^{\alpha}\Delta t_j\right]^{\beta-1}\times\tau_{i_i}^{\alpha}\Delta t_i$ | $\tau_{vm}$ | Zhang | $1.228\times10^{-7}$ | 1.9918 | 0.6606 |
| TH-8 | $D(\tau,t)=\frac{\Delta fHb}{Hb}=\sum_{i=inlet}^{i}C\beta\left[\sum_{j=1}^{j_i}\tau_{i_j}^{\alpha}\Delta t_j\right]^{\beta-1}\times\tau_{i_i}^{\alpha}\Delta t_i$ | $\tau_{b}$ | Zhang | $1.228\times10^{-7}$ | 1.9918 | 0.6606 |
| TH-9 | $D(\tau,t)=\frac{\Delta fHb}{Hb}=\sum_{i=inlet}^{i}C\beta\left[\sum_{j=1}^{j_i}\tau_{i_j}^{\alpha}\Delta t_j\right]^{\beta-1}\times\tau_{i_i}^{\alpha}\Delta t_i$ | $\tau_{p}$ | Zhang | $1.228\times10^{-7}$ | 1.9918 | 0.6606 |

**Table S1:** Equations and parameters for the hemolysis models studied.

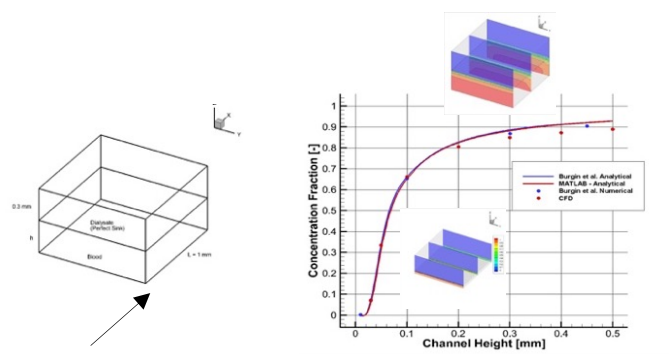


**Figure S1:** Verification and validation of the membrane transport model with data published in the literature (Burgin et al.)

| Parameter | Value | Units | Ref. |
|---|---|---|---|
| d | 15 | nm | [15] |
| $R_s$ | 0.36 | nm | [44] |
| $R_p$ | 5 | nm | [15] |
| $D_0$ | 1.16E-09 | m^2/s | [43] |
| $\phi$ | 0.05 | - | [15] |
| $D_m$ | 2.90E-11 | m^2/s | [15] |

**Table S2:** Properties of the molecule (urea) and membrane tested in the validation step[7], [37], [38].